Soft Matter

Cite this: *Soft Matter*, 2011, **7**, 2848

www.rsc.org/softmatter

PAPER

Pinning of domains for fluid–fluid phase separation in lipid bilayers with asymmetric dynamics

Waipot Ngamsaad,[ab] Sylvio May,*[a] Alexander J. Wagner[a] and Wannapong Triampo[c]

Received 2nd June 2010, Accepted 15th November 2010
DOI: 10.1039/c0sm00462f

We propose a physical mechanism for the arrest of domain coarsening in a system of two apposed two-dimensional binary fluids. The two fluids are subject to a dynamic asymmetry: strong friction with the environment allows domains in one fluid layer (the "bottom" fluid) to grow only diffusively, whereas hydrodynamic flow leads to initially faster growth in the apposed fluid (the "top" layer). The two fluids are energetically coupled so that domains of similar type interact favorably across the two fluids. Using lattice Boltzmann simulations we observe that at a certain length scale, which is independent of the coarsening state in the bottom layer, domain growth in the top layer comes to an arrest. A phenomenological model suggests the pinning of domains across the two fluids to cause the arrest in domain growth. The pinning results from the interplay between line tension and domain coupling strength across the two fluids. We apply our model to a lipid bilayer for which we calculate the length scale of the dynamically arrested domains in the top layer. We find domain extensions of about or somewhat larger than 20 nm. Potential applications of our pinning model are to mixed lipid bilayers that tend to phase separate and are subject to a dynamic asymmetry; these include model membranes on a solid support and lipid rafts in the plasma membrane.

Introduction

The dynamics of phase separation often controls the structure and properties of composite bulk materials such as binary alloys and polymer blends.[1,2] For two-dimensional fluid films interactions with the environment add an additional level of complexity. Here, lipid bilayers constitute the special type of *two* fluid layers that are, generally, coupled and interact with their environment. Each leaflet in a mixed lipid bilayer can be viewed as a fluid film that is able to undergo phase separation. The biological scope of this ability is embodied in the raft hypothesis,[3] where certain cholesterol-containing compositional domains with spatial extension ranging from several tens to few hundreds of nanometres have been associated with a wide range of cellular functions.[4]

From a basic physical viewpoint it is interesting to ask what the potential consequences of the coupling between the two leaflets in a lipid bilayer are. Here, coupling refers to the interaction of domains in one leaflet of the bilayer with domains in the apposed leaflet. The existence of such inter-leaflet coupling has been demonstrated and studied experimentally for a number of model systems, including symmetric[5] and asymmetric membranes.[6,7] Theoretical modeling predicts equilibrium phase diagrams that rationalize some of the experimental findings.[8,9]

Besides interacting with each other, the two leaflets of a lipid bilayer are also in contact with their environments. Different environments for the two leaflets entail consequences for the structural and dynamic membrane properties. For example, supported lipid bilayers are well known to exhibit essentially immobilized domains on relevant experimental time scales.[10,11] Although these domains exhibit fluid-like properties they appear static in time and no coalescence is observed. This is the case for large micrometre-sized domains but also for smaller sub-micrometre branched irregular networks of domains that have been observed using AFM microscopy.[12–14] Unlike for lipid monolayers on the air–water interface,[15] the observed domain structure in supported bilayers does not correspond to thermal equilibrium.

The asymmetric environments of a lipid bilayer and the emergence of finite-sized domains are also interesting aspects of biological membranes. Raft sizes in the plasma membrane are believed to be (roughly) in the range 20–100 nm. There are a number of possible lipid-based physical mechanism that restrict domain growth in the plasma membrane; they include the formation of transient domains through critical fluctuations,[16–18] non-equilibrium membrane recycling,[19,20] and the competition between short and long-range interactions between membrane domains.[21] Other mechanisms are protein-based, including the presence of immobilized protein obstacles created by cytoskeleton attachment sizes[22] and the fence and picket model,[23] where

[a]*Department of Physics, North Dakota State University, Fargo, North Dakota, 58105, USA*
[b]*School of Science, University of Phayao, Mueang Phayao, Phayao, 56000, Thailand*
[c]*Department of Physics, Faculty of Science, Mahidol University, Ratchathewi, Bangkok, 10400, Thailand*

transmembrane proteins line up along cytoskeletal protein fences thereby acting as rows of pickets that limit domain growth. For the latter two models the multitude of interactions of the cytoskeleton network (located exclusively inside the cell) with the inner leaf of the plasma membrane[24,25] introduces an asymmetry by restricting the mobility of the inner leaflet.

The presence of finite-sized domains in supported bilayers, and perhaps even the stability of membrane rafts, are a consequence of the asymmetric influence of the environment on the lipid bilayer. Below we suggest a general physical mechanism that predicts the appearance of dynamically stabilized domains, encountered under non-equilibrium conditions as a result of domain coarsening and resulting from a dynamic membrane asymmetry.

The two lipid monolayers that constitute a model membrane can be viewed as two coupled two-dimensional fluids, each with its own dynamical properties. Consider first a *single* two-dimensional binary fluid that is quenched into its unstable spinodal region. It phase-separates locally with subsequent coarsening of its domains according to the dynamic scaling hypothesis: the morphological structure remains statistically self-similar and can be described by the time evolution of a characteristic length scale $L(t)$. Introducing friction between the binary fluid and its environment generally slows down its phase-separation dynamics. Next, consider *two* two-dimensional fluids, one residing on top of the other (as in a lipid bilayer). Assume that friction with the environment is weaker for the top than for the bottom fluid (below, we completely neglect the friction with the environment for the top fluid). Phase coarsening of the two leaves of this fluid is then expected to proceed with different speeds. That is, the characteristic length in the top leaf, L_t, grows much faster than the characteristic length, L_b, in the apposed bottom leaf. Such a scenario would strictly apply if the two leaves of the bilayer were completely independent, *i.e.* with no inter-leaflet coupling of their domains. However, if the two apposed fluids are energetically coupled, their phase separation dynamics will differ from that of independent fluids layers.

In the present work we investigate the consequence of inter-leaflet coupling on domain coarsening of a bilayer with asymmetric dynamical properties. The bilayer consists of two apposed, binary, 1 : 1 fluid layers. It is asymmetric only in the sense that the dynamical properties of the bottom leaf are slowed down due to friction with the environment. To keep our model simple and instructive we will assume that the bilayer is symmetric in all other respects; *i.e.*, with chemically identical layers of the same composition). We will demonstrate that the presence of inter-leaflet coupling (*i.e.*, the presence of coupling between domains across the bilayer) leads, effectively, to a temporary arrest of the phase coarsening in the top leaf at a certain length scale $L_t = L_{pin}$. This length scale depends only on two material parameters of the bilayer but is independent of the domain structure in the bottom leaf. Lattice Boltzmann simulations of two apposed two-dimensional fluids and a phenomenological model indicate a non-equilibrium *pinning* mechanism that leads to the arrest of domain growth in the top fluid. We note that pinning mechanisms, such as contact line pinning or pinning due to chemically heterogeneous surfaces, have been studied intensively for three-dimensional systems [26]. In contrast, the present work considers domain pinning in a two-dimensional fluid where the pinning sites evolve from the slow dynamics of a second, apposed, fluid. Note that this situation is related to phase-separating fluids that contain immobile impurities. Here too, an arrest of domain growth was observed in previous simulations [27].

Model

Consider two apposed two-dimensional binary fluids (a "top" and a "bottom" fluid). The order parameter of the top layer is ϕ_t, and that of the bottom layer is ϕ_b. These order parameters are related to the concentration differences of the different lipids, as detailed in our previous publication,[8] so that the equilibrium phases correspond to $\phi_{t,b}^{eq} = \pm 1$. The densities ρ_t and ρ_b describe the total density in the top and bottom layer. For small Mach numbers considered here the density is nearly constant but small deviations in density are needed to represent the pressure in eqn (4) below.

We describe the free energy of the two apposed fluids using a Ginzburg–Landau free energy, supplemented by a quadratic coupling term that accounts for compositional differences between the layers

$$F = \int d\mathbf{a} \Big\{ c\rho_t \ln\rho_t - \frac{1}{2}\phi_t^2 + \frac{1}{4}\phi_t^4 + \frac{1}{2}(\nabla\phi_t)^2 + c\rho_b \ln\rho_b - \frac{1}{2}\phi_b^2 + \frac{1}{4}\phi_b^4 + \frac{1}{2}(\nabla\phi_b)^2 + \Lambda(\phi_t - \phi_b)^2 \Big\}. \quad (1)$$

Here, the integration runs over the lateral area of the bilayer, and all lengths are measured with respect to a conveniently chosen unit length. The prefactor c is a constant that we specify in the discussion following eqn (16) below; in our simulations we choose $c = 10/3$. The coupling parameter Λ controls the strength of the energetic interaction between compositional domains in the two layers.[28] The presence of inter-leaflet coupling influences the equilibrium phase behavior of two apposed asymmetric fluids. Specifically, there exists a critical coupling strength $\Lambda = \Lambda_c = 3/2$ that separates weak ($\Lambda < \Lambda_c$) and strong ($\Lambda > \Lambda_c$) coupling. The former but not the latter case exhibits three phase coexistence regions.[8,9]

Our central assumption in the present work is a dynamical asymmetry of the two apposed fluids. That is, friction of the top layer with its environment is much weaker than friction of the bottom layer with its environment. We implement this assumption into our model as a complete suppression of any flow within the bottom layer: Molecules (and hence domains) in the bottom fluid are able to diffuse but friction disables any flow in the bottom leaf. (We point out that the findings of this work would not be affected by the presence of some degree of hydrodynamic coarsening in the bottom layer as long as there is a marked dynamic asymmetry between the two fluids.) With the "no flow" condition, the dynamics of the order parameter of the bottom fluid ϕ_b is given by a simple Cahn–Hilliard equation

$$\partial_t \phi_b = \nabla[M_b \nabla \mu_{\phi_b}] \quad (2)$$

where M_b is the mobility and $\mu_{\phi_b} = \delta F/\delta\phi_b$ is the chemical potential. In contrast to the bottom fluid, the top fluid is able to evolve not only through diffusion but also through flow. This is

what introduces the dynamical asymmetry between the two layers. The top layer then satisfies an advected Cahn–Hilliard equation of the form

$$\partial_t\phi_t + \nabla(\phi_t\mathbf{u}_t) = \nabla[M_t\nabla\mu_{\phi_t}], \tag{3}$$

with the mobility M_t and chemical potential $\mu_{\phi_t} = \delta F/\delta\phi_t$. In addition, the velocity $\mathbf{u}_t$ of the top layer obeys the Navier–Stokes equation

$$\partial_t(\rho_t\mathbf{u}_t) + \nabla(\rho_t\mathbf{u}_t\mathbf{u}_t) = -\nabla p_t - \phi_t\nabla\mu_{\phi_t} + \mathbf{f}^t + \nabla\sigma_t. \tag{4}$$

Here $p_t = \rho_t/3$ is the pressure, $\sigma_t = \nu\rho_t[\nabla\mathbf{u}_t + (\nabla\mathbf{u}_t)^T]$ is a Newtonian stress tensor (where the superscript T denotes the transpose of a matrix), ν is the kinematic viscosity, and $\mathbf{f}^t = -\eta\mathbf{u}_t$ is the friction force between the two fluids, with the corresponding friction constant η. While our numerical method reproduces the full Navier–Stokes equations we only require the Stokes equations here,

$$\mathbf{f}^t + \nabla\sigma_t = c\nabla\rho_t + \phi_t\nabla\mu_{\phi_t}, \tag{5}$$

since the Reynolds number for our simulations is small ($Re \ll 1$) and inertial effects can therefore be neglected.

In this model we are neglecting fluctuations which would enter the Cahn–Hilliard equations as an additional current and in the Navier–Stokes equation as a fluctuating stress tensor and an additional fluctuating force corresponding to the inter-layer friction. These fluctuating forces and stresses are related to their corresponding dissipative forces through a fluctuation–dissipation theorem. While it will be interesting to investigate the effect of fluctuations in the future, they are outside the scope of this paper.

Numerical method

To simulate these equations we use a lattice Boltzmann (LB) method. Our method is based on the LB method for non-ideal fluids by Orlandini *et al.*[29] The Orlandini method simulated a two-component fluid mixture with an imposed free energy. This method was extended to examine bi-layer systems by considering two such fluid mixtures that are coupled through a forcing term related to the coupling free energy,[8] but it was assumed that there is no substrate but a strong frictional coupling between the layers so that the two layers do not have an independent hydrodynamic motion. Here we now assume that each layer has an independent hydrodynamic motion and they are coupled through a friction term proportional to the difference in local velocity in each layer.

Specifically we use four lattice Boltzmann equations, two each for the total mass density $\rho_{t,b}$ and order parameter ϕ for each layer. The lattice Boltzmann equation is an equation for densities f_i associated to velocities v_i. To keep the free energy in the dimensionless form of eqn (1) we choose a time step $\Delta t = 0.1$ and a lattice spacing of $\Delta x = \sqrt{2}/10$. The velocity set for our two-dimensional simulations is then given by $(0,0), (0,\pm\sqrt{2}), (\pm\sqrt{2},0), (\pm\sqrt{2},\pm\sqrt{2})$ for all possible permutations of the signs. The time evolution of the densities is governed by the lattice Boltzmann equation:

$$f_i^{(n)}(x + v_i\Delta t, t + \Delta t) = f_i^{(n)}(x,t) + \frac{1}{\tau^{(n)}}\left[f_i^{(n)0}\left(\rho^{(n)}, j^{(n)}, \Pi^{(n)}\right) - f_i^{(n)}(x,t)\right] + F_i^{(n)}, \tag{6}$$

where $\tau^{(n)}$ is a relaxation time (chosen as 1 for the simulations in this paper). The index n enumerates the lattice Boltzmann equations. We choose $n = 1$ for the total density of the top layer, $n = 2$ for the order parameter of the top layer, $n = 3$ for the total density of the bottom layer, and $n = 4$ for the order parameter of the bottom layer. This means we identify $\rho^{(0)} = \rho_t$, $\rho^{(1)} = \phi_t$, $\rho^{(3)} = \rho_b$, and $\rho^{(4)} = \phi_b$. The momentum for the top layer is $j^{(1)} = \rho_t u_t = \sum_i f_i^{(1)}(x,t)v_i$ and the momentum for the bottom layer is $j^{(3)} = \rho_b u_b = \sum_i f_i^{(3)}(x,t)v_i$. For the order parameters these terms are given by $j^{(2)} = \phi_t j^{(1)}/\rho_t$ and $j^{(4)} = \phi_b j^{(3)}/\rho_b$ respectively. The local pressure tensors are given by $\Pi^{(1)} = j^{(1)}j^{(1)}/\rho^{(1)} + P_t$, $\Pi^{(3)} = j^{(3)}j^{(3)}/\rho^{(3)} + P_b$ and $\Pi^{(2)} = \rho^{(2)}j^{(1)}j^{(1)}/(\rho^{(1)})^2 + \mu_{\phi_t}\mathbf{1}$, $\Pi^{(4)} = \rho^{(4)}j^{(3)}j^{(3)}/(\rho^{(3)})^2 + \mu_{\phi_b}\mathbf{1}$, where $\mathbf{1}$ represents a unit tensor. The pressure tensors P_t and P_b here are the single layer pressure tensors of the binary fluids, not including the interaction contributions. They are given by $P_t = [\rho_t/3 + \phi_t^2/2 + 3\phi_t^4/4 - \phi_t\nabla^2\phi_t - (\nabla\phi_t)^2/2]1 + \nabla\phi\nabla\phi$ for the top layer and an equivalent expression for P_b. The local equilibrium distribution is then given by

$$f^0(\rho,u,\Pi) = w_i\left[\rho\delta_{i0} + 3u.v_i + \frac{9}{2}\Pi : v_iv_i - \frac{3}{2}tr(\Pi)\right] \tag{7}$$

with weights $w_0 = 1$, $w_{1-4} = 1/9$ and $w_{5-8} = 1/36$. The $F_i^{(n)}$ represent the effect of the local force $F^{(n)}$ and are given by

$$F^{(n)} = w_i\left[3F^{(n)}.v_i + \frac{9}{2}\left(F^{(n)}u^{(n)} + u^{(n)}F^{(n)}\right) : v_iv_i - \frac{3}{2}\mathrm{tr}\left(F^{(n)}u^{(n)} + u^{(n)}F^{(n)}\right)\right] \tag{8}$$

As mentioned above we consider here the special case of a completely immobile bottom layer, *i.e.* $\boldsymbol{u}_b = 0$ in our simulations. The only relevant force is then the force on the top layer. It has two contributions: the friction between the two layers with a friction coefficient η and the interaction force due to the inter-leaflet coupling term:

$$F^{(1)} = \eta(u_b - u_t) + 2\Lambda\phi_t\nabla(\phi_b - \phi_t). \tag{9}$$

For numerical efficiency we consider the case of low friction between the layers in our simulations.

Simulations

We use our method to examine the phase-separation of a lipid bilayer with asymmetric dynamics. In particular we are interested in the phase-ordering dynamics as a function of the coupling strength Λ. We show a series of snapshots of a relatively small coupling parameter of $\Lambda = 0.0114$ in Fig. 1. We observe that the top layer does coarsen much faster initially. After about 5 000 iterations, however, the top morphology does essentially cease to coarsen and the evolution is almost entirely due to the slow diffusive growth of the bottom morphology. After about 500 000 iterations, the bottom morphology will match the top morphology and the two layers will coarsen together. Note, however, that this is an extremely slow process.

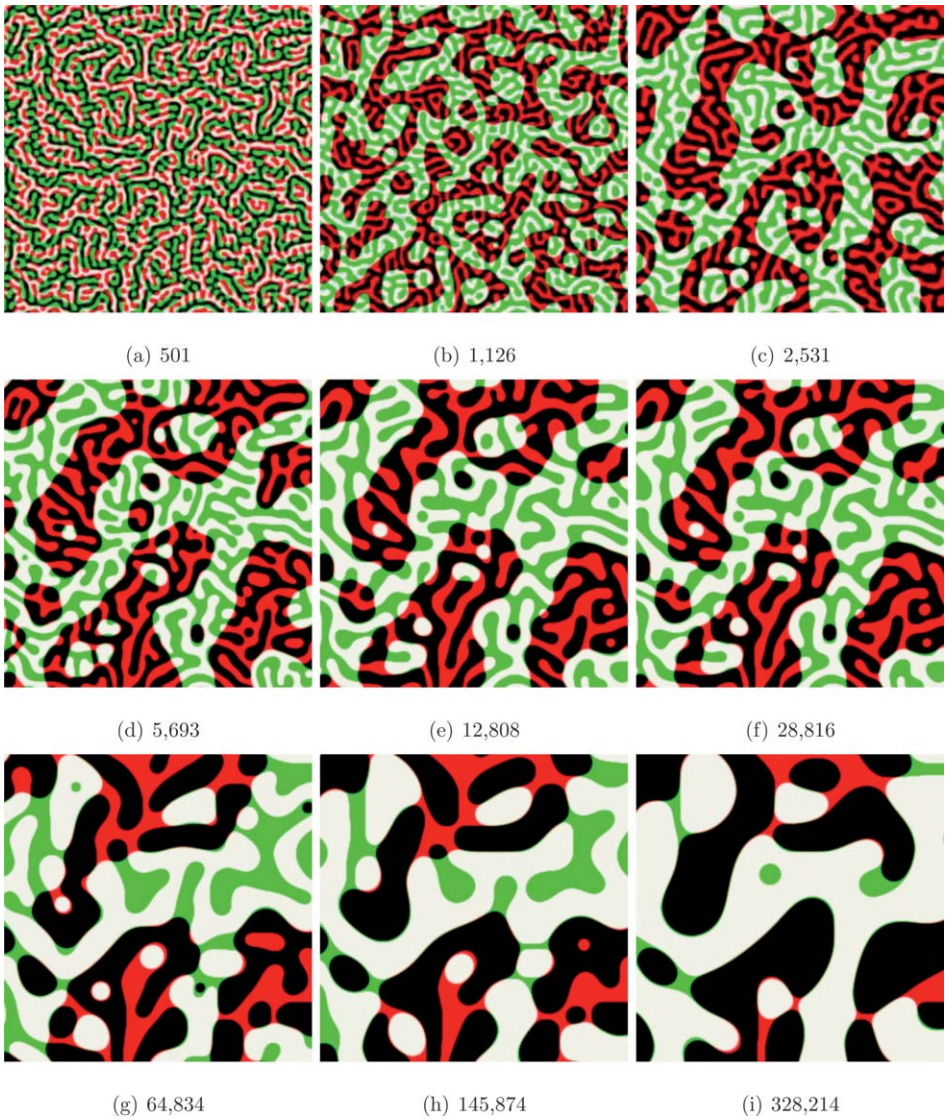

Fig. 1 Snapshots of a 300 × 300 section of the bilayer morphology at nine different times (measured as number of iterations). The full simulation size was 1800 × 1800. The images are composite images including information about both the top and the bottom layer. The A-rich-A-rich phase labeled white, B-rich-B-rich phase labeled black, A-rich-B-rich phase labeled green, and B-rich-A-rich phase labeled red. The coupling parameter is $\Lambda = 0.0114$.

What is the underlying mechanism for this apparent freezing of the top morphology? Let us first consider the limiting case of no coupling. In this situation the two layers will coarsen independently. The bottom layer will coarsen entirely diffusively. The diffusive coarsening dynamics obeys the dynamics scaling hypotheses, *i.e.* morphologies at a later time are statistically identical to morphologies at an earlier time if they are scaled by an appropriate length scale $L(t)$. For these diffusive systems the appropriate growth law is the power law $L \propto t^{1/3}$. The top layer will coarsen hydrodynamically which leads to much faster growth. Unfortunately the dynamic scaling hypothesis is not valid for binary fluids in two dimensions.[30] Instead of a statistically similar picture where later times simply correspond to larger length-scales, here more and more near-circular drops are enclosed in the larger non-circular domains. This is illustrated in Fig. 2. Simple dimensional scaling analysis suggests that if the scaling hypothesis was correct one should find a $L \propto t$ scaling law, as is indeed found in three dimensions. Furukawa[31] argued that even in two dimensions one can recover this scaling law if one considers only the largest domains that do not constitute circular domains.

We measure the length-scale $L(t)$ in our simulations by measuring the length of the interface $L_I(t)$ separating the domains in a simulation box of extensions L_x and L_y. One measure of the characteristic length-scale $L(t)$ is given by[30]

$$L(t) = \frac{L_x L_y}{L_I(t)}. \tag{10}$$

We measured the evolution of this length scale for the top and bottom morphology for a number of different coupling parameters, and some of these results are shown in Fig. 3. Let us first consider the evolution in the absence of coupling (*i.e.* $\Lambda = 0$). There appears an initial fast coarsening in the top layer consistent with the $L \propto t$ scaling prediction followed by a slowdown and a coarsening rate that more closely resembles $L \propto t^{1/3}$.

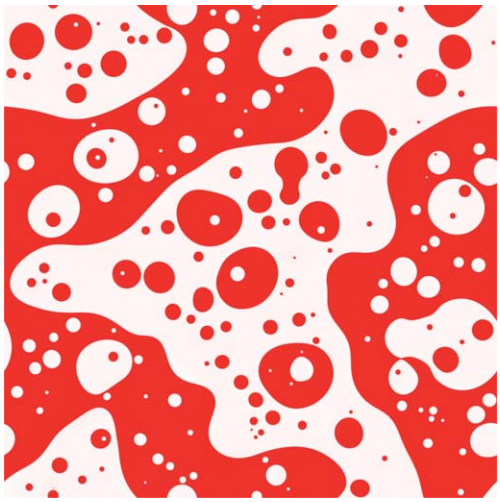

Fig. 2 Top layer morphology of uncoupled ($\Lambda = 0$) hydrodynamic coarsening after 43 223 iterations in a simulation with 1800×1800 lattice points. We observe that the largest length scale is already close to the system size. Within these large domains many smaller circular domains have accumulated, leading to the violation of the dynamic scaling hypothesis.

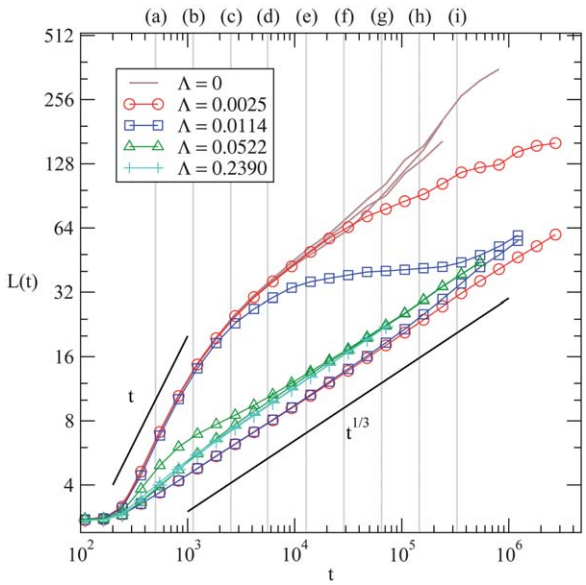

Fig. 3 Log–log plot of the characteristic length-scale L, defined in eqn (10), for the top and bottom layers. Results for five different coupling parameters Λ are shown. The two curves for each Λ correspond to L_t (upper curve) and L_b (lower curve). For $\Lambda = 0$ we show three runs that differ only in the initial noise, which allows us to estimate the variance of different simulations. For large domain sizes there is a visible spread in the data. Vertical lines with letters (a)–(i) indicate the times for which snapshots are shown in Fig. 1 for $\Lambda = 0.0114$ (blue squares).

However, such an argument is difficult to make since finite size effects start to become important very early into the apparent $L \propto t^{1/3}$ regime (see Fig. 2) even for the comparatively large system size of 1800×1800. These finite size effects are also noticeable in the variability of simulations with different initial random noise, shown in Fig. 3.

Even in the absence of a clear theoretical understanding of two-dimensional hydrodynamic coarsening we can examine the effect that a coupling to the bottom layer through the coupling parameter Λ has. In Fig. 3 we show results for different coupling parameters Λ. For each simulation there are two lines, one corresponding to the top layer and one corresponding to the bottom layer. We notice that the bottom layer does indeed coarsen with the $L \propto 1/3$ power law, as expected. The influence of the coupling parameter is minor, but becomes noticeable for larger values of the coupling parameter where we observe that the coarsening of the bottom layer is accelerated by about a factor of about 1.25. We return to a discussion of this effect below.

For small coupling parameters the initial coarsening of the top layer will follow the behavior of the uncoupled system. However, at some length-scale a slowing down of the coarsening is observed. The larger the coupling parameter is, the sooner the transition occurs until, for coupling parameters above $\Lambda \gtrsim 0.02$, the morphologies are so strongly coupled that the length-scales of the two layers never diverge. Let us consider the case of $\Lambda = 0.0114$ for which we already discussed the morphology evolution in Fig. 1. In the length scale graph of Fig. 3 we see that the length scale $L(t;\Lambda = 0.0114)$ starts to diverge from $L(t;\Lambda = 0)$ at around $t \approx 2000$ and a length of $L \approx 25$. From direct comparison with Fig. 1 we see that coarsening is not completely arrested by this time. But by time 5000 the morphology is clearly pinned. The length scale also reaches a plateau around $L \approx 32$ and essentially stays there while the bottom morphology continues to coarsen virtually unaffected by the top morphology. Around time $t \approx 10^6$ the bottom morphology reaches the size of the top morphology. From Fig. 1 we see that at this point both morphologies overlap. Looking closely we see that the coarsening of the bottom morphology actually accelerates once its domains reach a size of about half of the domain size of the pinned top morphology.

A similar acceleration of the diffusive coarsening is also observed for larger coupling constants of $\Lambda = 0.0522$ and 0.239.

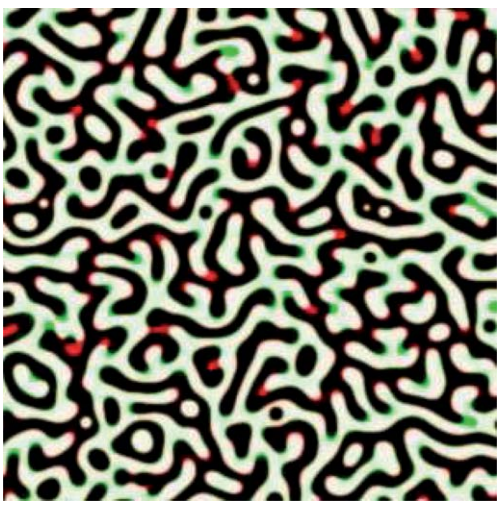

Fig. 4 Nearly overlapping domains for $\Lambda = 0.0522$ after 2 531 iterations in a 300×300 subpart of the 1000×1000 lattice. Coloring-scheme is the same as in Fig. 1. Note that the top domains are leading the bottom domains in the coarsening, *i.e.* that the mean curvature for the top domains is less than that for the bottom domains.

To understand why this is happening let us examine such a nearly overlapping morphology in some more detail. In Fig. 4 we see two nearly identical morphologies. Although small, the differences are important. Note that the black and green domains, representing the bottom morphology have a higher curvature. The black and red domains, representing the top morphology are somewhat less curved. The faster hydrodynamic domains of the top layer are slightly ahead in coarsening of the domains in the bottom layer which are only coarsening diffusively. So why does this lead to an accelerated coarsening of the bottom layer? Not only does the coupling pin the top layer, preventing the domains to coarsen quickly. The slight mismatch of the domains in the top influences the bottom layer and the diffusive dynamics work not only to reduce the interface of the bottom layer, but also to match the top layer. More formally this is the effect of Λ which enters the chemical potential in eqn (2). This leads to enhanced diffusion in the areas where the top domains are moving ahead of the bottom domain. But recall that hydrodynamic coarsening in two dimensions leads to a violation of dynamic scaling because hydrodynamics can help make domains round, but does nothing to round domains, so that they still have to coarsen diffusively. This mechanism leads to the accumulation of droplets so noticeable in Fig. 2. Does the enhanced diffusive coarsening in the bottom layer lead to the same effect?

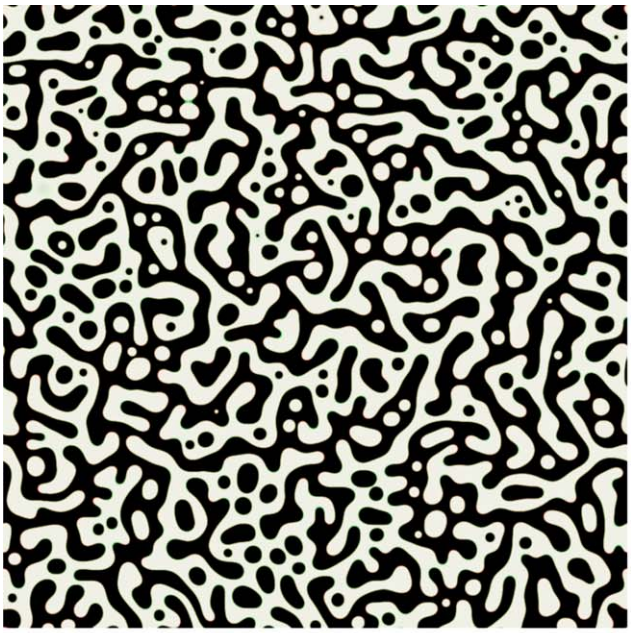

(a) $\Lambda = 0.0522$

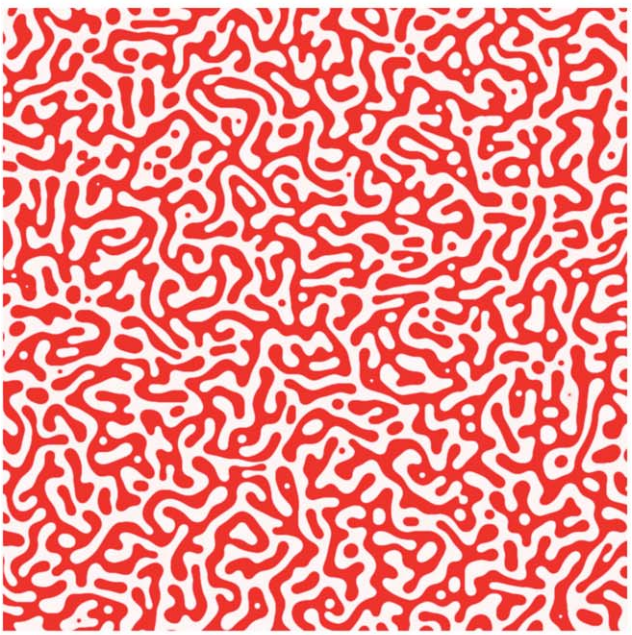

(b) $\Lambda = 0$

Fig. 5 Comparison of a strong coupling morphology ($\Lambda = 0.0522$) which has an accelerated growth with a purely diffusive morphology ($\Lambda = 0$). Both images are taken after 43 223 iterations and show a 1000×1000 section. Note that the coupling in (a) leads to larger domains as well as an accumulation of circular domains, reminiscent of hydrodynamic coarsening.

To answer this question let us now consider the same system at a later time. In Fig. 5 (a) we see the domains after 43 223 iterations. In this 1000×1000 image the mismatch of the top and bottom morphologies is nearly invisible. (In the top left corner of the image in Fig. 5 (a) there are two drops which have just merged in the top layer whereas they are still separate in the bottom layer). We compare this image with an identical diffusive system without coupling shown in Fig. 5 (b). The uncoupled system is known to obey the dynamic scaling law. Firstly we notice that the enhanced coarsening leads to noticeably larger domains. We already obtained this information in Fig. 3 by noticing the larger length scales due to enhanced coarsening. But another feature is evident: the morphology obtained with enhanced diffusive coarsening does indeed contain many more

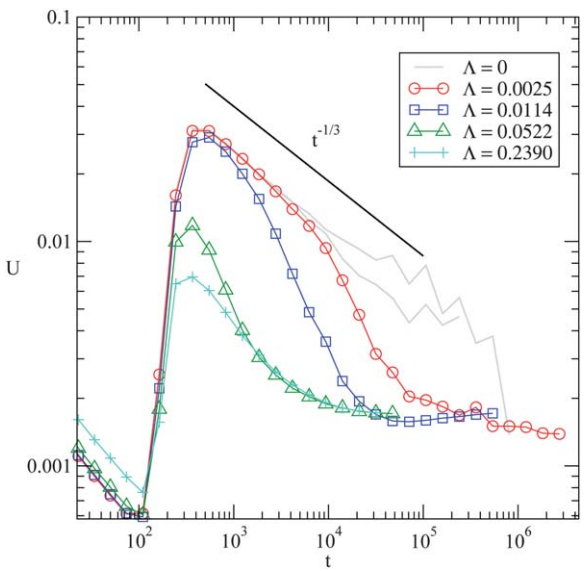

Fig. 6 Log–log plot of the characteristic velocity U for the top layers. Results for five different coupling parameters Λ are shown. For $\Lambda = 0$ we show two runs that differ only in the initial noise, which allows us to estimate the variance of different simulations. For large domain sizes there is a visible spread in the data.

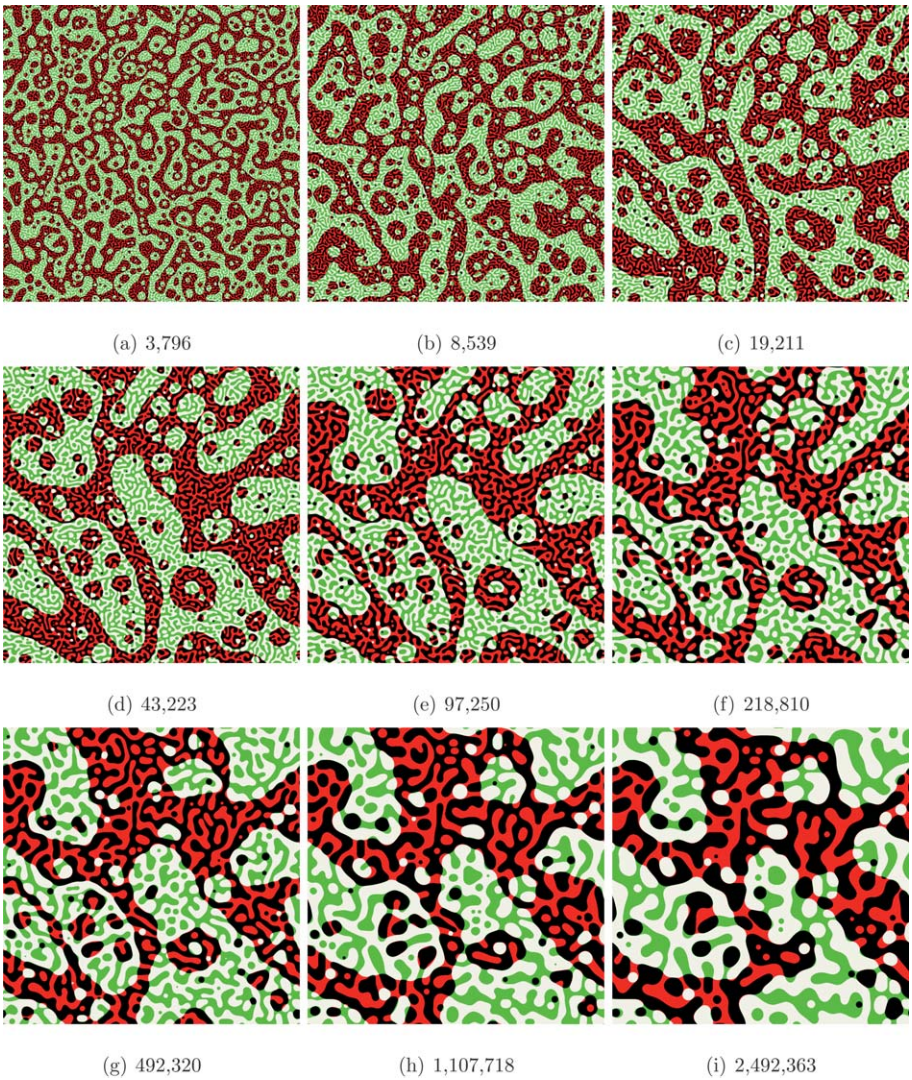

Fig. 7 Snapshots of the bilayer morphology at nine different times (measured as number of iterations) for a simulation size of 1800×1800. The images are composite images as in Fig. 1. The coupling parameter is $\Lambda = 0.0025$. Note that the large-scale features of the top morphology are pinned after about 40 000 iterations. This corresponds to the point where the length scale measure in Fig. 3 starts to diverge from the results for $\Lambda = 0$.

circular domains. This suggests that dynamic scaling will also be violated for these diffusively coarsening morphologies.

We can also study the coarsening behavior by examining the fluid velocity, responsible for hydrodynamic coarsening. Since in hydrodynamic coarsening fluid flow is responsible for the growth of the domains we would expect that a typical velocity scale would behave as $u \propto dL/dt$. If we had viscous hydrodynamic growth and dynamical scaling was valid we would therefore expect that the $L \propto t$ growth law leads to a constant typical fluid velocity. Even if the dynamical scaling hypothesis were to hold only for the largest domains[31] one might expect that the scaling of the velocity would continue to hold true. To examine this we measured the typical velocity defined as

$$U = \frac{\sum_x |\mathbf{u}(\mathbf{x}, \mathbf{t})|}{L_x L_y}. \tag{11}$$

The observed velocities are shown in Fig. 6. In our simulations we find that the typical velocity is not a constant, even for $\Lambda = 0$. At the onset of coarsening the typical velocity rapidly increases. However, after a maximum is reached, the velocity decreases. The decrease is consistent with a power-law $U \propto t^{-1/3}$. We speculate that the decrease of the typical fluid velocity may be due to the increased apparent viscosity of the large domains due to the inclusion of many smaller domains.

For finite values of the coupling parameter Λ the velocity initially follows the $\Lambda = 0$ case. After some time we then observe a marked decrease of the velocity compared to the decoupled case. The divergence of the length scales and the velocities occurs at essentially the same time, giving us two measures for when the pinning process starts. For our later analysis it would be more useful to obtain a pinning length scale. However, given the breakdown of the dynamic scaling hypothesis, this is not a well defined process. Consider *e.g.* the morphology in Fig. 2. The length scale measure of eqn (10) suggests that the typical length scale is about 80 for this morphology. But the typical length scale of the large domains, which is the relevant length scale for the

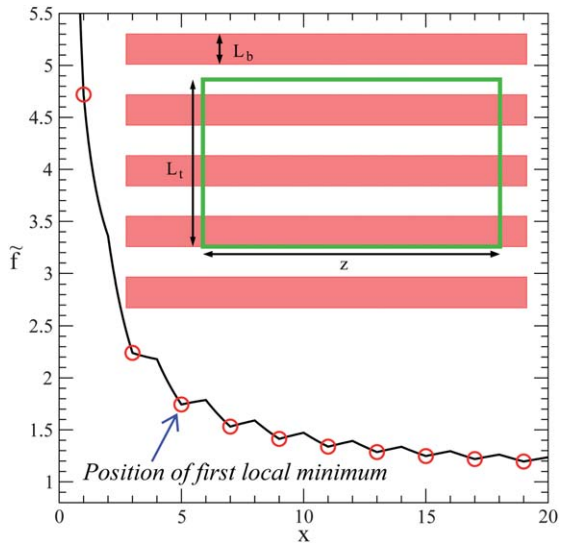

Fig. 8 Domain free energy according to our simplified analytical model, displayed for $\bar{\sigma} = 2.37$. Open circles indicate positions where the ratio L_t/L_b is an odd integer; of those only local minima are potential pinning states. The first minimum occurs at $x = L_t/L_b = 5$. The corresponding pinning length, $L_{pin} = \sigma/\Lambda = 38$, is in agreement with our simulation result; see Fig. 9.

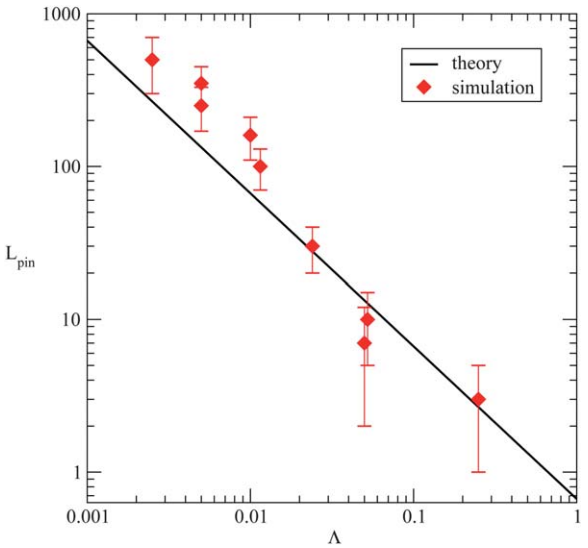

Fig. 9 Comparison of the measured pinning length with the pinning length observed in our simulations. There is good qualitative agreement with theory, although our simple theory appears to underestimate the pinning length in more complex situations by somewhat less than a factor of 2.

arrest of hydrodynamics through the pinning mechanism, is of the order of 500.

This discrepancy also raises the question as to when exactly pinning becomes important. In Fig. 3 we see that for the case of $\Lambda = 0.0025$ there is a divergence from the length scale observed for $\Lambda = 0$ at around $t \approx 30\,000$, but not a length scale plateau, as seen for $\Lambda = 0.0114$. So is there actual pinning observed for $\Lambda = 0.0025$? To answer that question we return to the real-space images of the morphologies. These are shown in Fig. 7. Examining this time evolution we see that the top domains are initially growing, but after the snapshot at $t = 43\,000$ the largest length scales do no longer grow. There is still a noticeable evolution for the small enclosed droplet domains, which continue to join or evaporate, but the largest structures undergo very few major rearrangements. So it is reasonable to state that we observe pinning of the large domains, despite the fact that the length scale measure of eqn (10) continues to grow, as shown in Fig. 3. In the next section we consider the physical origin of the pinning mechanism.

Analytical model for pinning

The physical origin of the arrest in phase coarsening can be understood on the basis of a simple analytical model. Let us represent the domain structure of the bottom layer by a pattern of long, linear, equidistant, parallel stripes of thickness L_b; see inset of Fig. 8. The order parameter adopts the equilibrium values, $\phi_b = \pm 1$, alternating between subsequent stripes.

Note that the restriction of the bottom layer's dynamics to diffusive motion effectively renders L_b statically fixed. Assume that also the top layer contains a pattern of long stripes with thickness $L_t > L_b$, and consider the rectangular section of a single stripe with fixed area A, corresponding length $z = A/L_t$, and order parameter $\phi_t = -1$. The interfacial energy of the rectangular section is $2\sigma z$ where the free energy in eqn (1) implies a line tension $\sigma = \sqrt{8}/3$ (which, strictly, requires the coupling constant Λ to be small). The second contribution to the free energy originates in the domain coupling across the two apposed fluids. This is expressed by the mismatch energy, $\Lambda \int_A d\mathbf{a}(\phi_t - \phi_b)^2$ (see the last term in eqn (1)), which yields $4\Lambda L_b z N$. Here, the function $N = N(L_t/L_b)$ denotes the number of non-matching stripes (with $\phi_b = +1$) contained in A. Partial overlap implies non-integer N. To calculate N we assume, without loss of generality, that the lower face of the rectangular section always aligns with the interface of a matching stripe in the bottom fluid; see inset of Fig. 8. The number of stripes can then be expressed as a function of the ratio $x = L_t/L_b$ through

$$N(x) = I\left(\frac{x}{2}\right) + 2\max\left\{R\left(\frac{x}{2}\right), \frac{1}{2}\right\} - 1 \qquad (12)$$

where $I(x)$ is the integer part of x and $R(x) = x - I(x)$ is the remainder. The sum of line tension and domain mismatch energy is thus

$$F = 2\sigma z + 4\Lambda L_b z N(L_t/L_b). \qquad (13)$$

Noting the conservation of stripe area $A = zL_t$, defining both the dimensionless energy $\tilde{f} = F/(2A\Lambda)$ and line tension $\tilde{\sigma} = \sigma/(2L_b\Lambda)$, and using $x = L_t/L_b$ leads to $f(x) = 2[\tilde{\sigma} + N(x)]/x$ which is plotted in Fig. 8 for $\tilde{\sigma} = 2.37$. Each local minimum corresponds to a metastable domain size. That is, for a small deformation the reduction in interfacial free energy is less than the increase in free energy due to the domain mismatch. Local minima appear only above a sufficiently large x. Hence, initial growth of the top domain will terminate in the first local minimum which is located at $x = 2I(\tilde{\sigma}) + 1$. For large x this becomes $x = 2\tilde{\sigma}$, corresponding to a domain size $L_t = L_{pin}$ with

$$L_{\mathrm{pin}} = \frac{\sigma}{\Lambda}. \tag{14}$$

Note that L_{pin} depends only on the line tension and coupling parameter but is independent of the characteristic length L_{b} in the bottom layer. Hence, arrest of domain growth in the top layer occurs at fixed L_{pin}, irrespective of how far coarsening within the bottom layer has progressed.

To compare our theory to the simulation results we measured the pinning length by examining the largest length scales in our pinned simulations by hand. This is not a well-defined process and leads to a significant error. The measurements are particularly challenging for large coupling parameters where the pinning occurs at a length-scale close to the initial spinodal length scale. However, one can certainly find the length-scale within about a factor of 2 or so with this method. The results of this comparison are shown in Fig. 9. We find that there is fairly good agreement between our simple theory and simulations. We estimate that our theory will underestimate the pinning length by about a factor of two. Presumably this is due to the simplification of a regular striped pattern rather than a complex spinodal decomposition pattern that allows for more freedom in the coarsening of the top domains.

Discussion

Our analysis reveals a *dynamic stabilization of microdomains* in the top leaflet during the process of phase coarsening. After the quenching of the two fluid layers into an unstable region of the phase diagram, domains in the top layer initially grow faster than in the bottom layer, the difference arising from the difference in friction of the two fluid layers with their respective environments. However, at a (scaled) characteristic size L_{pin} (see eqn (14)) the domain growth in the top layer stops due to a *pinning mechanism* with the smaller domains in the bottom leaf. Remarkably, the arrest in domain growth is independent of the domain size in the bottom layer and thus persists until the domains in the bottom layer have *diffusively* grown to match those in the top layer (Fig. 1 (i)).

The characteristic length scale of the microdomains follows from the scaled free energy in eqn (1), namely $L_{\mathrm{pin}} = \sigma/\Lambda$; see eqn (14). Recall that $\sigma = \sqrt{8}/3$ and Λ are both dimensionless (scaled) quantities, and so is L_{pin}. In the following we scale L_{pin} back to be measured in meters. To make the procedure transparent we recall the scaled free energy corresponding to one of the two layers, top ($\rho \to \rho_{\mathrm{t}}$and $\phi \to \phi_{\mathrm{t}}$) or bottom ($\rho \to \rho_{\mathrm{b}}$and $\phi \to \phi_{\mathrm{b}}$), according to eqn (1),

$$F_{\mathrm{t/b}} = \int d\mathbf{a}\left\{c\rho\ln\rho - \frac{1}{2}\phi^2 + \frac{1}{4}\phi^4 + \frac{1}{2}(\nabla\phi)^2 + \Lambda\phi^2\right\} \tag{15}$$

Eqn (15) can be viewed as the scaled version of a corresponding unscaled free energy $F'_{\mathrm{t/b}}$ (where here and below unscaled quantities carry a prime) with

$$\frac{F'_{\mathrm{t/b}}}{k_BT} = \int d\mathbf{a}'\rho'\left\{\ln\rho' + \phi'_{\mathrm{t}}\ln\phi'_{\mathrm{t}} + \left(1-\phi'_{\mathrm{t}}\right)\ln\left(1-\phi'_{\mathrm{t}}\right) + \chi'\phi'_{\mathrm{t}}\left(1-\phi'_{\mathrm{t}}\right) + K'(\nabla\phi')^2 + \Lambda'\left(\phi'_{\mathrm{t}}\right)^2\right\} \tag{16}$$

Here, $\rho'$and ϕ' are, respectively, the total area density (unit m^{-2}) and the mole fraction (dimensionless) of the fluid layer, $k_BT$is the thermal energy, χ'(dimensionless) characterizes the nonideality of the binary fluid, K' (unit m^2) is the rigidity with respect to compositional gradients, and Λ' (dimensionless) is the inter-leaflet coupling parameter. We note that eqn (16) is valid within the Bragg–Williams approximation of a binary lattice gas; see also ref. 8. For $\chi' > 2$ the fluid layer phase separates. If χ' remains sufficiently close to 2, eqn (16) implies the equilibrium mole fractions $\phi' = \phi'_{\mathrm{eq}}$ with $\phi'_{\mathrm{eq}} = 1/2 \pm \sqrt{3(\chi'-2)/8}$ and a line tension of $k_BT\sigma' = \rho' k_BT(\chi'-2)^2\xi'/2$ where $\xi' = \sqrt{2K'/(\chi'-2)}$ is the characteristic decay length of the interfacial profile $\phi'(x') = 1/2 + \sqrt{3(\chi'-2)/8}\tanh(x'/\xi')$ along a direction x' normal to a phase boundary. To transform from $F'_{\mathrm{t/b}}$ to $F_{\mathrm{t/b}}$, we rescale the area $a = \alpha a'$ (the unit of α is m^{-2}), the energy $F_{\mathrm{t/b}} = \gamma F'_{\mathrm{t/b}}/(3k_BT)$, and the mole fraction $\phi = (\phi' - 1/2)/b$, leading to $\alpha = (\chi'-2)/K'$, $\gamma = 4/[(\chi'-2)K'\rho']$, $b^2 = 3(\chi'-2)/8$, $\Lambda = \Lambda'/[2(\chi'-2)]$, and $c = 4/[3(\chi'-2)^2]$. Using these transformation rules we can show that the scaled line tension becomes $\sigma = \sigma'\gamma/(3\sqrt{\alpha}) = \sqrt{8}/3$. More importantly, we can express the scaled pinning length L_{pin} in eqn (14) in its unscaled form as $L'_{\mathrm{pin}} = L_{\mathrm{pin}}/\sqrt{\alpha} = 2\sqrt{8K'(\chi'-2)}/(3\Lambda')$ or, equivalently, as

$$L'_{\mathrm{pin}} = \frac{\sigma'}{\Lambda'\rho'\left(\phi'_{\mathrm{eq}} - 1/2\right)^2} \tag{17}$$

The arrest of domain growth analyzed in our present work is a general phenomenon for dynamically asymmetric and energetically coupled fluid layers. Yet, we find it particularly interesting to discuss the arrest of domain growth in the context of lipid bilayers. Collins[32] has argued that, roughly, the inter-leaf domain coupling parameter Λ' can be estimated as $\Lambda' \lesssim \sigma'/(\rho' d')$ where $d' \approx 5$ nm is the thickness of a lipid bilayer membrane, and $k_BT\sigma'$ is the line tension between membrane domains. Typical values of the line tension between membrane domains are $k_BT\sigma' = 1$–10 pN,[33] and the cross-sectional area per lipid is roughly $1/\rho' \approx 0.7\ \mathrm{nm}^2$. With that Collins' prediction amounts to $\Lambda' \lesssim \sigma'/(\rho' d') = 0.1$–$1$ which is in good agreement with detailed molecular dynamics simulations (based on a coarse grained model) that resulted in $\Lambda' = 0.1$–0.2.[34] Inserting Collins' estimate into eqn (17) yields $L'_{\mathrm{pin}} \gtrsim d'/(\phi'_{\mathrm{eq}} - 1/2)^2$. Because the equilibrium mole fraction of the phase separated fluid layer must fulfil the relation $|\phi'_{\mathrm{eq}} - 1/2| < 0.5$ we obtain $L'_{\mathrm{pin}} \gtrsim 20$ nm. It is interesting to note that this length is at the lower end of reported sizes of rafts in the plasma membrane. This could suggest that the dynamic arrest of domain growth adds an additional mechanism to the ones (listed in the Introduction) that have been suggested recently. What our mechanism requires is a dynamic asymmetry of the bilayer membrane. For the plasma membrane such asymmetry could be introduced through the coupling of the cytoplasmic face of the membrane with the cytoskeleton.[35] We finally note that also for supported model membranes a dynamic asymmetry may be introduced through the presence of the solid support.

In conclusion, we have investigated the dynamics of phase coarsening for two coupled two-dimensional binary fluids. Both fluids are initially identical 1 : 1 mixtures with one fluid exhibiting slow dynamics. This implies for the other fluid a temporary arrest of its phase coarsening. The arrest reflects the pinning of

the large domains by the small ones in the apposed fluid. For lipid bilayers the characteristic length scale of the arrested domains is $L_{pin} \gtrsim 20$ nm. We suggest that this pinning mechanism may potentially contribute to the dynamics of domain coarsening in supported bilayers and raft formation in the plasma membrane.

Acknowledgements

We acknowledge support from the Thailand Research Fund and the Thailand Center of Excellence in Physics (WN and WT), from the Faculty of Science at Mahidol University (WT), from NIH through Grant GM077184 (SM), and ND EPSCoR SEED grant (AJW). We also thank Julia Yeomans, Anna Balazs, and David Andelman for illuminating discussions and Eric Foard for parallizing our numerical code.

References

1 A. Shinozaki and Y. Oono, *Phys. Rev. E*, 1993, **48**(4), 2622–2654.
2 K. Binder, *Adv. Polym. Sci.*, 1994, **112**, 181–299.
3 K. Simons and E. Ikonen, *Nature*, 1997, **387**(6633), 569–572.
4 K. Simons and W. L. C. Vaz, *Annu. Rev. Biophys. Biomol. Struct.*, 2004, **33**, 269–295.
5 J. Korlach, P. Schwille, W. W. Webb and G. W. Feigenson, *Proc. Natl. Acad. Sci. U. S. A.*, 1999, **96**(15), 8461–8466.
6 M. D. Collins and S. L. Keller, *Proc. Natl. Acad. Sci. U. S. A.*, 2008, **105**(1), 124–128.
7 C. Wan, V. Kiessling and L. K. Tamm, *Biochemistry*, 2008, **47**(7), 2190–2198.
8 A. J. Wagner, S. Loew and S. May, *Biophys. J.*, 2007, **93**(12), 4268–4277.
9 G. G. Putzel and M. Schick, *Biophys. J.*, 2008, **94**(3), 869–877.
10 B. L. Stottrup, S. L. Veatch and S. L. Keller, *Biophys. J.*, 2004, **86**, 2942–2950.
11 C. Dietrich, L. A. Bagatolli, Z. N. Volovyk, N. L. Thompson, M. Levi, K. Jacobson and E. Gratton, *Biophys. J.*, 2001, **80**(3), 1417–1428.
12 B. Y. van Duyl, D. Ganchev, V. Chupin, B. de Kruijff and J. A. Killian, *FEBS Lett.*, 2003, **547**(1–3), 101–106.
13 L. J. Johnston, *Langmuir*, 2007, **23**(11), 5886–5895.
14 M. H. Jensen, E. J. Morris and A. C. Simonsen, *Langmuir*, 2007, **23**(15), 8135–8141.
15 Y. F. Hu, K. Meleson and J. Israelachvili, *Biophys. J.*, 2006, **91**(2), 444–453.
16 S. L. Veatch, O. Soubias, S. L. Keller and K. Gawrisch, *Proc. Natl. Acad. Sci. U. S. A.*, 2007, **104**(45), 17650–17655.
17 S. L. Veatch, P. Cicuta, P. Sengupta, A. Honerkamp-Smith, D. Holowka and B. Baird, *ACS Chem. Biol.*, 2008, **3**(5), 287–293.
18 A. R. Honerkamp-Smith, S. L. Veatch and S. L. Keller, *Biochim. Biophys. Acta, Biomembr.*, 2009, **1788**(1), 53–63.
19 J. Fan, M. Sammalkorpi and M. Haataja, *Phys. Rev. Lett.*, 2008, **100**(17), 178102.
20 J. Gomez, F. Sagues and R. Reigada, *Phys. Rev. E*, 2008, **77**(2), 021907.
21 N. Destainville, *Phys. Rev. E*, 2008, **77**, 011905.
22 A. Yethiraj and J. C. Weisshaar, *Biophys. J.*, 2007, **93**(9), 3113–3119.
23 A. Kusumi, C. Nakada, K. Ritchie, K. Murase, K. Suzuki, H. Murakoshi, R. S. Kasai, J. Kondo and T. Fujiwara, *Annu. Rev. Biophys. Biomol. Struct.*, 2005, **34**, 351–U54.
24 A. Viola and N. Gupta, *Nat. Rev. Immunol.*, 2007, **7**(11), 889–896.
25 G. R. Chichili and W. Rodgers, *Cell. Mol. Life Sci.*, 2009, **66**(14), 2319–2328.
26 S. Herminghaus, M. Brinkmann and R. Seemann, *Annu. Rev. Mater. Res.*, 2008, **38**, 101–121.
27 F. Qiu, G. Peng, V. V. Ginzburg, A. C. Balaz, H.-Y. Chen and D. Jasnow, *J. Chem. Phys.*, 2001, **115**, 3779–3784.
28 P. L. Hansen, J. H. Ipsen and L. Miao, *Phys. Rev. E.*, 1998, **58**, 2311–2324.
29 E. Orlandini, M. R. Swift and J. M. Yeomans, *Europhys. Lett.*, 1995, **32**(6), 463–468.
30 A. J. Wagner and J. M. Yeomans, *Phys. Rev. Lett.*, 1998, **80**(7), 1429–1432.
31 H. Furukawa, *Phys. Rev. E*, 2000, **61**(2), 1423–1431.
32 M. D. Collins, *Biophys. J.*, 2008, **94**(5), L32–L34.
33 A. W. Tian, C. Johnson, W. Wang and T. Baumgart, *Phys. Rev. Lett.*, 2007, **98**(20), 208102.
34 S. J. Marrink, A. H. de Vries, T. A. Harroun, J. Katsaras and S. R. Wassall, *J. Am. Chem. Soc.*, 2008, **130**(1), 10–11.
35 A. Kusumi, H. Ike, C. Nakada, K. Murase and T. Fujiwara, *Seminars in Immunology*, 2005, **17**(1), 3–21.